

Core–Shell Nanorods for Efficient Photoelectrochemical Hydrogen Production

Z. G. Yu,^{*,†} C. E. Pryor,[‡] W. H. Lau,[§] M. A. Berding,[†] and D. B. MacQueen[†]

SRI International, 333 Ravenswood Avenue, Menlo Park, California 94025, Optical Science and Technology Center and Department of Physics and Astronomy, University of Iowa, Iowa City, Iowa 52242, and Center for Spintronics and Quantum Computation and Department of Physics, University of California, Santa Barbara, California 93106

Received: September 14, 2005; In Final Form: October 13, 2005

We propose core–shell InP–CdS and InP–ZnTe nanorods as photoelectrodes in the efficient photoelectrochemical hydrogen production. On the basis of our systematic study using strain-dependent k,p theory, we find that in these heterostructures both energies and wave function distributions of electrons and holes can be favorably tailored to a considerable extent by exploiting the interplay between quantum confinement and strain. Consequently, these core–shell nanorods with proper dimensions (height, core radius, and shell thickness) can simultaneously satisfy all criteria for effective photoelectrodes in solar-based hydrogen production.

I. Introduction

Splitting water using a photoelectrochemical (PEC) process for efficient hydrogen production is a promising approach that can ultimately solve the energy problem facing humanity.¹ In the PEC process, a semiconductor material absorbs light, resulting in the generation of electron–hole pairs, and thus serves as a photoelectrode. These electrons and holes, instead of running through a circuit, as in photovoltaics, are consumed at the semiconductor–electrolyte interface to effect the splitting of water into hydrogen and oxygen. After several decades' effort, however, the solar-to-hydrogen efficiency remains too low for PEC hydrogen production to be cost-effective for large-scale applications.² The major obstacle is to find a suitable semiconductor material to serve as a photoelectrode that simultaneously satisfies four stringent requirements: (1) The semiconductor material must have a band gap in the range 1.5–2.0 eV to capture most of the photons in the solar spectrum. (2) The conduction and valence band edges, or the lowest unoccupied molecular orbital (LUMO) and highest occupied molecular orbital (HOMO), of the materials must overlap the H₂/H₂O and O₂/H₂O redox potentials to provide the free energy needed under H₂/O₂ evolution conditions. (3) Charge transfer across the semiconductor–liquid interface must be fast compared to the electron–hole recombination. (4) The semiconductor surface must be chemically stable in the aqueous medium.³ For a bulk material, the band edges and their relative positions with respect to H₂O redox potentials are intrinsic material properties and can be modified externally only to a limited extent.⁴ Hence, considerable efforts in the field of PEC hydrogen production have been devoted to searching for a material that fortuitously meets these four criteria. To date, semiconductor photoelectrodes with a demonstrated high efficiency in splitting water have large band gaps and only make use of the ultraviolet portion of the solar spectrum.⁵ On the other hand, semiconductors with smaller band gaps that better match the solar spectral distribution either

corrode or become inert in the aqueous media.⁵ One of the best photoelectrodes identified for hydrogen production to date is p-type GaInP₂, which has a band gap of 1.8–1.9 eV.⁶ However, its band edges are too negative to effect photoelectrolysis, and more seriously, the material is unstable and susceptible to corrosion in water.^{7,8}

The advent of nanotechnology opens new avenues to discovering and synthesizing improved semiconductor photoelectrodes for hydrogen production. Nanostructures have been frequently used to obtain large surface-to-volume ratios,⁹ and ultrafine nanoparticles have been explored to modify the local electron polarization and spatially separate photogenerated electrons and holes.¹⁰ However, the most fundamental and fascinating aspect of nanostructures, quantum confinement, has not yet been seriously utilized in PEC hydrogen production. Since all of the aforementioned criteria are essentially controlled by the underlying electronic structure of the material, exploiting quantum confinement will in principle enable one to tailor a nanostructure to meet these criteria. We note, however, that simply reducing the size of a single material to the nanometer scale, which in general increases the band gap, is usually not helpful in hydrogen production. This is because for the photoelectrodes stable in water the gap is already too large, whereas for semiconductors with smaller band gaps the quantum confinement does not address the problem of reactivity in water. Here, we suggest that nano-heterostructures are the places where one can best exploit quantum confinement and strain to effectively tailor the electronic structures for hydrogen production while simultaneously addressing the stability in water.

In this paper, we study core–shell nanorods and examine their electronic structures and wave functions against all of the criteria for an effective photoelectrode in PEC hydrogen production. Core–shell nanospheres, while intensively studied, are unsuitable for PEC hydrogen production (as will be shown in the next section). Having scrutinized many nanostructures made of various semiconductors, we find that InP–CdS and InP–ZnTe core–shell nanorods can be tailored to satisfy all of these criteria and therefore are promising nano-photoelectrodes. In section II of this paper, we describe our design of core–shell nanorods for hydrogen production. In section III, we

* To whom correspondence should be addressed. E-mail: zhi-gang.yu@sri.com.

† SRI International.

‡ University of Iowa.

§ University of California, Santa Barbara.

present our theoretical approach. Section IV is devoted to discussions of results on core–shell InP–CdS and InP–ZnTe nanorods. Finally, we summarize our conclusions in section V.

II. Core–Shell Nanorods for Hydrogen Production

To identify materials and structures as efficient photoelectrodes for hydrogen production, we begin with a common semiconductor with a band gap close to the desired value, for example, InP (1.4 eV). To protect it from corrosion in the aqueous environment, we can coat it with a shell to form a core–shell heterostructure. The shell must be stable in water and have a large band gap so that most photons in the solar spectrum can penetrate into the core for absorption and creation of electron–hole pairs. Once an electron–hole pair is created in the core, it should have a sufficiently long lifetime to complete the redox reactions before the electron and the hole recombine. The most effective way to reduce such a recombination is to spatially separate the electron and the hole immediately upon creation, which can be achieved in a heterostructure with so-called type-II band alignment. In a system with type-II band alignment, the conduction and valence band edges of the smaller band gap material are not within the gap of the larger band gap material. In the core–shell structures considered here, where the core has a smaller gap than the shell, type-II band alignment occurs if either the conduction band edge in the shell is lower than that in the core or the valence band edge in the shell is higher than that in the core. In the former situation, the electron (LUMO) tends to stay in the shell to lower its energy, while the hole (HOMO) remains in the core, whereas, in the latter situation, the LUMO is distributed in the core, while the HOMO is in the shell.

We emphasize that a very strong type-II band alignment (i.e., a large discontinuity in either the conduction or valence band edge) is not beneficial for hydrogen production, because it will necessitate a much larger band gap in the core than that required to facilitate the redox reactions, thereby reducing the solar-to-hydrogen efficiency. Thus, it is desirable that the core–shell structure have a weak type-II band alignment with either the conduction band edge or the valence band edge being similar across the system, which not only retains a high solar-to-hydrogen efficiency but also provides strong quantum confinement effects in tailoring the electronic structures.

Since the HOMO and LUMO of a system often do not overlap the water redox potentials, it is necessary that the HOMO and LUMO can be tuned either upward or downward. Simply reducing the system size is not an economical approach to improve the overlap, since it pushes the HOMO and LUMO to opposite directions, which significantly increases the gap and consequently reduces the solar-to-hydrogen efficiency. A more efficient way is to shift the HOMO and LUMO in the same direction or independently, which can be achieved in a structure where the HOMO and LUMO are spatially separated, as will be shown below.

Finally, to maintain a fast hydrogen and oxygen production, both electrons and holes must transfer from the photoelectrode into the solution quickly and therefore both the core and the shell must be accessible from the solution. This requirement renders spherical core–shell structures, which have been extensively studied both theoretically and experimentally,^{11–13} unsuitable for PEC hydrogen production, although they are useful in many other applications. Having taken into consideration all of these aspects, we identify the core–shell InP–CdS and InP–ZnTe nanorods as efficient photoelectrodes in hydrogen production. In the InP–CdS nanorods, the conduction band

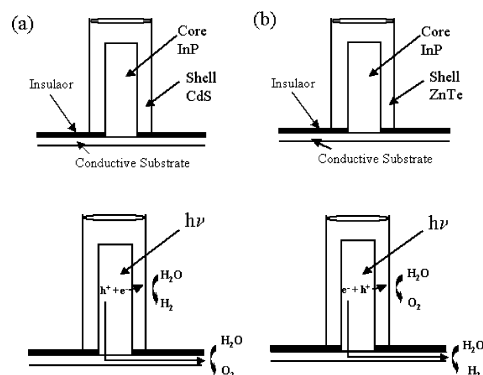


Figure 1. Schematic device structures showing the core–shell InP–CdS (a) and InP–ZnTe (b) nanorods used in hydrogen production. First, InP rods are grown on a conductive substrate to form cores; then, an insulator layer is deposited on the substrate. Finally, CdS or ZnTe is grown to cover the InP cores and form the core–shell nanorods.

edges in the core and in the shell are similar. In the InP–ZnTe nanorods, the valence band edges in different regions are similar.

The envisioned device structures based on the core–shell InP–CdS and InP–ZnTe nanorods for hydrogen production are illustrated in Figure 1. The shell in such a structure can serve as the anode (cathode) in the electrochemical process of hydrogen production if the hole (electron) is localized in the shell, at whose surface oxygen (hydrogen) is generated. The core is connected to the cathode (anode) through a conductive substrate, on which the structure is grown, to facilitate hydrogen (oxygen) generation. To minimize the interference between electron and hole charge transfer processes, an insulator layer is grown between the shell material and the conductive substrate. For the InP–CdS structure in Figure 1a, electrons are localized in the shell and holes in the core, whereas, for the InP–ZnTe structure in Figure 1b, electrons are in the core and holes in the shell.

Recent advances in the synthesis of nanoparticles and nanostructures give promise of successful fabrication of the proposed device structures in Figure 1. In particular, high-quality InP nanocrystals with different shapes and dimensions have been synthesized by colloidal chemistry methods²⁴ and further coated by a variety of II–VI materials including CdS, ZnSe, and CdSe with controlled thickness to form core–shell spheres.²⁵ Possible unpassivated dangling bonds on the surface of the nanorods, which may give rise to undesirable localized states that trap photogenerated electrons and holes, can adversely affect the performance of these photoelectrodes. However, it has been demonstrated that such unpassivated dangling bonds can be effectively eliminated by etching processes.²⁴

III. Theoretical Approach

Due to the lattice mismatch between the materials comprising a core–shell nanorod, the calculation of electronic properties requires a method that accounts for the strain-induced modification of the semiconductor band structure. Nanorod calculations are done numerically, using a well-established technique that has been used for the study of self-assembled strained quantum dots.¹⁴ First, the strain is calculated using linear continuum elastic theory¹⁵ and the finite element method. The calculated strain is then used as input to a real-space strain-dependent $k \cdot p$ Hamiltonian, using four bands for the valence states and a single-band effective mass model for the conduction states.

The strain distribution in a structure with lattice mismatched materials is obtained by minimizing the elastic energy, given by

$$F = \int d^3x \frac{1}{2} C_{xxxx} (\sigma_{xx}^2 + \sigma_{yy}^2 + \sigma_{zz}^2) + C_{xyxy} (\sigma_{xx} \sigma_{yy} + \sigma_{xx} \sigma_{zz} + \sigma_{yy} \sigma_{zz}) + 2C_{xyxy} (\sigma_{xy}^2 + \sigma_{xz}^2 + \sigma_{yz}^2) - \alpha (\sigma_{xx} + \sigma_{yy} + \sigma_{zz}) \quad (1)$$

where σ_{ij} is the strain tensor, the C 's are material-dependent elastic constants, and α is a parameter used to enforce the lattice mismatch between the two materials. The strain is given in terms of the displacement by $\sigma_{ij} = (1/2)(\partial_i u_j + \partial_j u_i)$. F is constructed as a function of the u 's on a cubic grid with derivatives replaced by differences and then minimized using the conjugate gradient algorithm.

Because the materials to be studied in this paper lack inversion symmetry, the strain produces a polarization given by $P_i = e_{ijk} \sigma_{jk}$, leading to an additional electrostatic potential. For zinc blende semiconductors, the only nonzero elements of the piezoelectric tensor are $e_{xyz} = e_{zyx} = e_{yxz} \equiv e_{14}$. From the polarization, we can compute the electrostatic potential (V_p) by numerically solving the Poisson equation.

The electronic states are computed by Lanczos diagonalization of a real-space representation of the $k.p$ Hamiltonian on a cubic grid. For the conduction band states, the Hamiltonian is¹⁶

$$H_c = E_c - \frac{\hbar^2}{2m_c} (\partial_x^2 + \partial_y^2 + \partial_z^2) + a_c (\sigma_{xx} + \sigma_{yy} + \sigma_{zz}) - eV_p \quad (2)$$

where E_c is the conduction band edge of the unstrained system, a_c is the conduction band hydrostatic deformation potential, and m_c is the effective mass of conduction band electrons. To determine the valence band states, we diagonalize the four-band strain-dependent Hamiltonian¹⁶

$$H_v = H_v^k + H_v^s - eV_p \quad (3)$$

where

$$H_v^k = - \begin{pmatrix} P - Q & S^* & -R & 0 \\ S & P + Q & 0 & -R \\ -R^* & 0 & P + Q & -S^* \\ 0 & -R^* & -S & P - Q \end{pmatrix} \quad (4)$$

$$H_v^s = - \begin{pmatrix} p + q + u & s^* + v^* & -r - w & 0 \\ s + v & p + q + u & 0 & -r - w \\ -r^* - w^* & 0 & p + q + u & -s^* - v^* \\ 0 & -r^* - w^* & -s - v & p - q + u \end{pmatrix} \quad (5)$$

$$P = -E_v - \gamma_1^L \frac{\hbar}{2m_0} (\partial_x^2 + \partial_y^2 + \partial_z^2)$$

$$Q = \gamma_2^L \frac{\hbar}{2m_0} (2\partial_z^2 - \partial_x^2 - \partial_y^2)$$

$$R = \frac{\sqrt{3}\hbar}{2m_0} [\gamma_2^L (\partial_x^2 - \partial_y^2) - 2i\gamma_3^L \partial_x \partial_y]$$

$$S = -\sqrt{3}\gamma_3^L \frac{\hbar}{m_0} \partial_z (\partial_x - i\partial_y)$$

$$p = a_v (\sigma_{xx} + \sigma_{yy} + \sigma_{zz})$$

$$q = b \left[\sigma_{zz} - \frac{1}{2} (\sigma_{xx} + \sigma_{yy}) \right]$$

$$s = -d (\sigma_{xz} - i\sigma_{yz})$$

$$r = \frac{\sqrt{3}}{2} b (\sigma_{xx} - \sigma_{yy}) - id\sigma_{xy}$$

$$u = -\frac{\Delta}{3} (\sigma_{xx} + \sigma_{yy} + \sigma_{zz})$$

$$v = -\frac{2\Delta}{3\sqrt{3}} (\sigma_{xz} - i\sigma_{yz})$$

$$w = -i \frac{2\Delta}{3\sqrt{3}} \sigma_{xy} \quad (6)$$

Here, E_v is the valence band edge of the unstrained system, γ_i^L ($i = 1, 2, 3$) are the Luttinger parameters, m_0 is the free electron mass, a_v is the valence band hydrostatic deformation potential, Δ is the spin–orbit coupling, and b and d are shear deformation potentials. The values of these parameters used in the calculations are summarized in Table 1. Here, we consider only zinc blende CdS and ZnTe.

Having obtained the eigenstates in the conduction and valence bands, we can calculate the binding energy (E_b) of an electron–hole pair due to the Coulomb interaction

$$E_b = \int d\mathbf{r}_1 \int d\mathbf{r}_2 \frac{|\psi_e(\mathbf{r}_1)|^2 |\psi_h(\mathbf{r}_2)|^2}{\bar{\epsilon}_0 |\mathbf{r}_1 - \mathbf{r}_2|} \quad (7)$$

where ψ_e and ψ_h are the eigenfunctions of a conduction electron and a valence electron, respectively, and $\bar{\epsilon}_0$ is the dielectric constant of the system, which is approximated in the calculations to be the simple average of the dielectric constants for the core and shell materials, $\bar{\epsilon}_0 = (\epsilon_0^{\text{core}} + \epsilon_0^{\text{shell}})/2$.

IV. Results and Discussion

In this section, we discuss in detail the electronic structures and wave functions as well as their dependence on the dimensions of InP–CdS and InP–ZnTe nanorods. To simplify our calculations while still capturing the essential physics, we consider coaxial, open-ended cylindrical core–shell nanorods, although, in practice, the core at one end of the nanorod is capped by the shell material, as illustrated in Figure 1. In the calculations, a cylindrical rod is arranged in such a way that its axis is along the z -axis, and the plane of $z = 0$ is located at the half-height of the rod. The cylindrical coordinates (r, θ, z) are

TABLE 1: Material Parameters Used in the Calculations^{17–23}

parameter	InP	CdS	ZnTe
m_c	0.0790 m_0	0.173 m_0	0.16 m_0
γ_1^L	5.08	2.2	3.44
γ_2^L	1.60	0.35	0.59
γ_3^L	2.10	1.53	2.03
E_g (eV)	1.42	2.56	2.39
E_c (eV)	0.48	0.90	1.16
E_v (eV)	−0.94	−1.60	−1.23
Δ (eV)	0.108	0.0	1.0
a_c (eV)	−6.0	−3.59	−6.95
a_v (eV)	−0.6	−1.51	−2.28
b (eV)	−2.0	−0.5	−1.2
d (eV)	−5.0	−3.7	−5.5
e_{14}	0.035	0.21	0.028
C_{11} (GPa)	101.1	77.9	71.3
C_{12} (GPa)	56.1	52.7	40.7
C_{44} (GPa)	45.6	24.1	31.2
a	0.586 97	0.582	0.610
ϵ_0	12.5	8.5	10.4

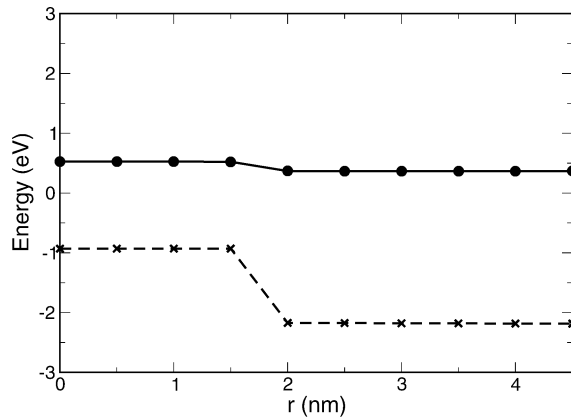


Figure 2. Conduction (solid line) and valence (dashed line) band edges for a core–shell InP–CdS nanorod with $H = 10$ nm, $R = 5$ nm, and $R_1 = 2$ nm. The circles and crosses represent the computational grid points at which the material is specified.

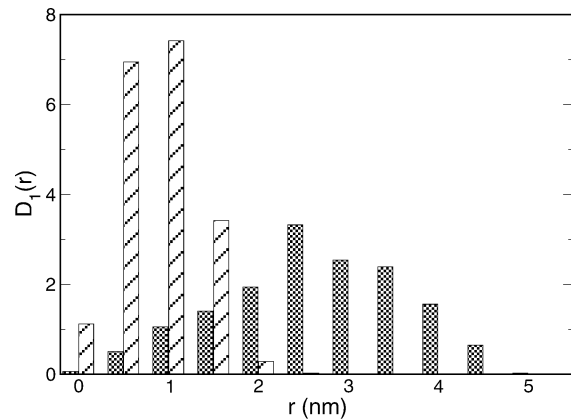


Figure 3. Radial charge distribution, $D_1(r)$, of the HOMO (striped bars) and the LUMO (shaded bars) in the same structure as that in Figure 2.

used throughout the paper. We denote the core radius as R_1 , the overall radius as R , and the height as H . The thickness of the shell is thus $d \equiv R - R_1$.

A. Core–Shell InP–CdS Nanorods. First, we show a typical band alignment of a core–shell InP–CdS nanorod. These band edges are obtained by minimizing the elastic energy due to strain and neglecting the kinetic energy of the electrons. Such band edges can be regarded as spatially dependent potentials for the valence and conduction electrons. We plot in Figure 2 the conduction and valence band edges along the radial direction in the plane of $z = 0$ for an InP–CdS nanorod with $R = 5$ nm, $H = 10$ nm, and $R_1 = 2$ nm. It should be noted that the band alignment depends on the strain and therefore is a function of dimensions of the structure. We see from Figure 2 that this nanorod exhibits a weak type-II band alignment, with the conduction band edge in the shell being slightly lower than that in the core. Thus, in this structure, once an electron–hole pair is created in the core by photoexcitation, the electron (LUMO) tends to migrate to the shell while the hole (HOMO) remains in the core.

To demonstrate the spatial separation of electrons and holes, we define a radial charge distribution, $D_1(r)$, for an eigenstate, ψ ,

$$D_1(r) = \int dz \int d\theta r |\psi(r, \theta, z)|^2 \quad (8)$$

Figure 3 displays the radial charge distribution of the HOMO and LUMO. We see that the HOMO is predominantly distrib-

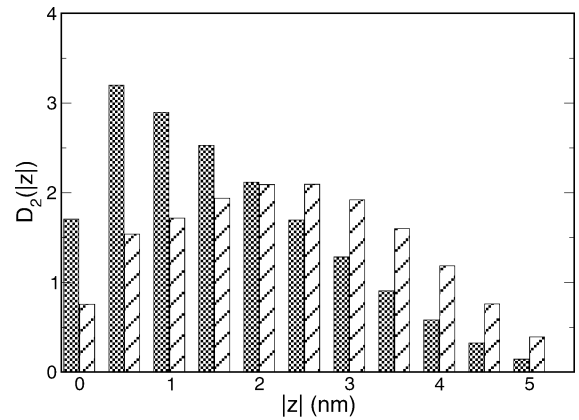


Figure 4. Charge distributions of the HOMO (striped bars) and LUMO (shaded bars) along the z -axis in the same core–shell InP–CdS nanorod as that in Figure 2.

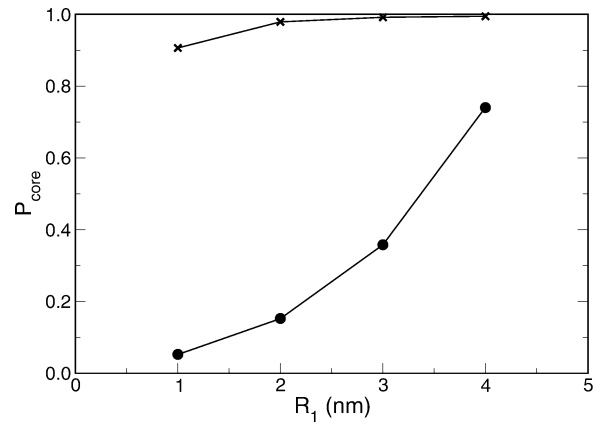


Figure 5. Integrated charge distribution in the core (P_{core}) for the HOMO (crosses) and the LUMO (circles) as a function of R_1 in core–shell InP–CdS nanorods with fixed $R = 5$ nm and $H = 2$ nm.

uted within the core ($r < 2$ nm), whereas the LUMO is mainly localized in the shell ($2 \text{ nm} < r < 5$ nm). These distributions clearly indicate the spatial separation of the HOMO and LUMO.

Moreover, the HOMO and LUMO also have different distributions along the z -axis. The distribution function along the z -axis is defined as

$$D_2(|z|) = 2 \int dr \int d\theta |\psi(r, \theta, z)|^2 \quad (9)$$

We see from Figure 4 that the LUMO is mostly localized in the center of the nanorod ($|z| < 2$ nm), whereas the HOMO is localized outside the center ($|z| > 2$ nm). The different charge distributions of the HOMO and LUMO along the z -axis can be used to enhance their spatial separation to achieve faster charge transfer dynamics.

In a core–shell InP–CdS nanorod, both the charge distributions and the energies of the HOMO and LUMO can be tuned to a considerable degree by adjusting the dimensions of the structure. We define the integrated charge distribution in the core for an eigenstate as

$$P_{\text{core}} = \frac{\int_0^{R_1} dr D_1(r)}{\int_0^R dr D_1(r)} \quad (10)$$

which measures whether an eigenstate is mainly in the core ($P_{\text{core}} > 0.5$) or in the shell ($P_{\text{core}} < 0.5$). Figure 5 shows the P_{core} values of the HOMO and LUMO as a function of core radius (R_1) in InP–CdS nanorods with a fixed height of $H = 2$

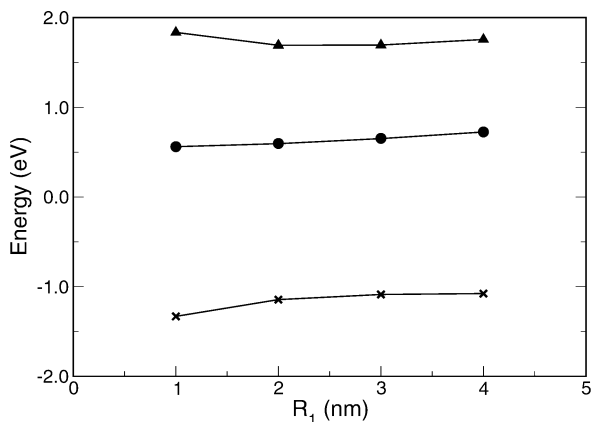


Figure 6. Energies of the HOMO (crosses) and LUMO (circles) as well as the energy gap (E_g) (triangles) as a function of R_1 in the same structure as that in Figure 5.

nm and an overall radius of $R = 5$ nm. We see that, as the core radius increases and the shell thickness decreases (because of the fixed R), the system undergoes a transition. At small core radii, the HOMO and the LUMO are well separated, with the HOMO predominantly in the core and the LUMO in the shell. With increase of the core radius, the LUMO gradually moves from the shell to the core, and eventually, both the HOMO and the LUMO become localized in the core. This transition is understandable because, as the core radius increases and the shell thickness decreases, the LUMO, initially localized in the shell, will feel a stronger quantum confinement, which in turn increases the electron kinetic energy. When the increased kinetic energy overcomes the conduction-band-edge offset between the core and the shell, the LUMO will have a lower energy in the core.

Spatial separation of photogenerated electrons and holes can greatly reduce their recombination (both radiative and nonradiative) probability. Although an accurate determination of the recombination rate requires a detailed computation of transition matrix elements, the recombination rate is approximately proportional to the square of the wave function overlap between the HOMO and the LUMO (Φ^2) which can be estimated from the P_{core} values of these states via

$$\Phi^2 \approx P_{\text{core}}^{\text{H}} P_{\text{core}}^{\text{L}} + (1 - P_{\text{core}}^{\text{H}})(1 - P_{\text{core}}^{\text{L}}) \quad (11)$$

where $P_{\text{core}}^{\text{H}}$ and $P_{\text{core}}^{\text{L}}$ are the P_{core} values for the HOMO and LUMO, respectively. For the InP–CdS nanorods described in Figure 5, Φ^2 changes from 0.74 at $R_1 = 4$ nm, where both the HOMO and the LUMO are localized in the core, to 0.14 at $R_1 = 1$ nm, where the HOMO and LUMO are spatially separated, indicating that the recombination lifetime can be significantly extended (5-fold) through the spatial separation of the HOMO and LUMO.

Apart from the charge distribution, the quantum confinement effects also change the energies of the HOMO and LUMO. We plot in Figure 6 the HOMO energy (E_{H}), the LUMO energy (E_{L}), and the energy gap (E_g) as a function of R_1 in InP–CdS nanorods with fixed $H = 2$ nm and $R = 5$ nm. The gap in these heterostructures is actually the lowest exciton (electron–hole pair) energy, which can be calculated by

$$E_g = E_{\text{L}} - E_{\text{H}} - |E_{\text{b}}| \quad (12)$$

where E_{b} is the binding energy resulting from the Coulomb interaction between the electron in the LUMO and the hole in the HOMO. E_g is the energy that will be used toward

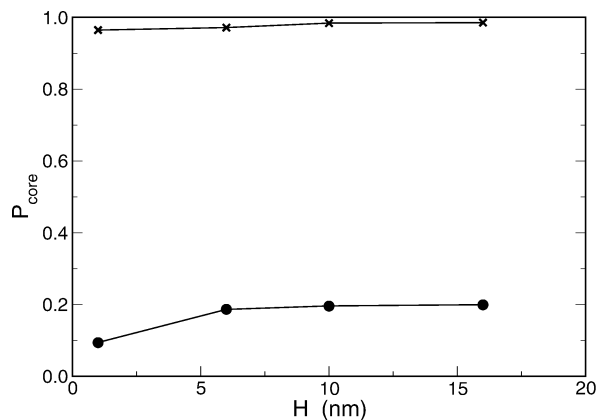


Figure 7. Integrated charge distribution in the core (P_{core}) for the HOMO (crosses) and the LUMO (circles) as a function of H of core–shell InP–CdS nanorods with fixed $R_1 = 2$ nm and $R = 5$ nm.

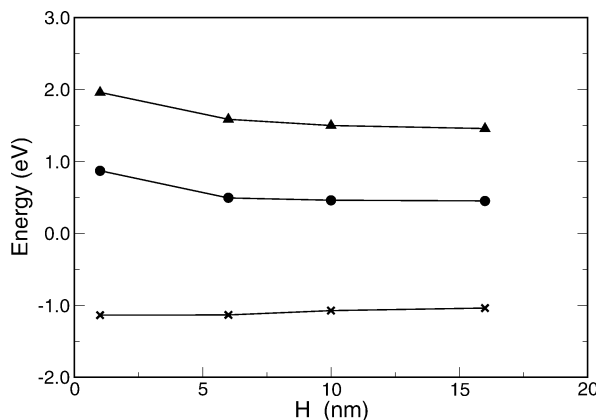


Figure 8. Energies of the HOMO (crosses) and LUMO (circles) as well as the energy gap (E_g) (triangles) as a function of H in the same structure as that in Figure 7.

electrolyzing water and thus is an important property in hydrogen production. From Figure 6, we see that, as the core radius decreases from $R_1 = 4$ nm to $R_1 = 1$ nm, the HOMO energy changes from -1.08 to -1.33 eV and the LUMO changes from 0.72 to 0.56 eV. Both energy changes are large enough to satisfy the overlap requirement in most situations,⁷ although for the HOMO the change is more pronounced. More importantly, these energy changes are in the *same* direction, meaning that both the HOMO and LUMO can shift upward (downward) by increasing (reducing) the core radius to improve their overlap with H_2O redox potentials without significantly increasing the gap, which is an outstanding attribute of the InP–CdS nanorods as photoelectrodes.

The quantum confinement effects also manifest themselves when the height of an InP–CdS nanorod varies. We depict P_{core} for the HOMO and LUMO in Figure 7 and the energies E_{L} , E_{H} , and E_g in Figure 8 as a function of H of InP–CdS nanorods with fixed $R_1 = 2$ nm and $R = 5$ nm. Figure 7 shows that as the height decreases the HOMO remains predominantly localized in the core, while the LUMO is concentrated in the shell and the charge density in the shell ($1 - P_{\text{core}}$) is slightly enhanced. The smaller change of charge localization along the z -axis, as compared to that along the radial direction, is due to the enhancement or reduction of quantum confinement for both the core and the shell when the height varies. Figure 8 indicates that as the height of the nanorod decreases from $H = 16$ nm to $H = 1$ nm, the HOMO energy changes from -1.04 to -1.14 eV, while the LUMO changes from 0.45 to 0.87 eV. Since the change in the LUMO energy is much more significant than that

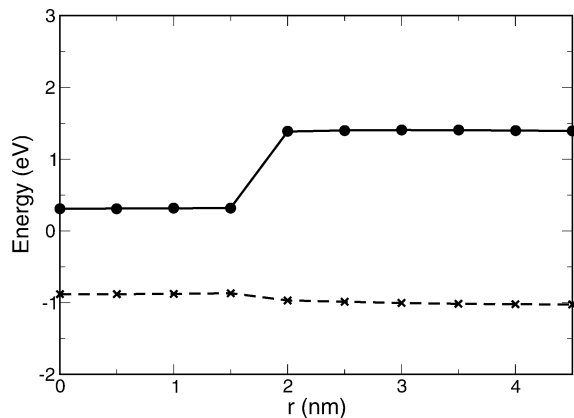


Figure 9. Conduction (solid line) and valence (dashed line) band alignments for a core-shell InP-ZnTe nanorod with $H = 10$ nm, $R = 5$ nm, and $R_1 = 2$ nm. The circles and crosses represent the computational grid points at which the material is specified.

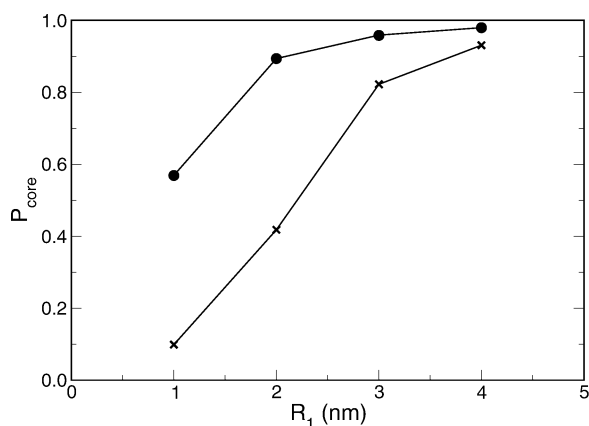


Figure 10. Integrated charge distribution in the core (P_{core}) for the HOMO (crosses) and the LUMO (circles) as a function of R_1 of core-shell InP-ZnTe nanorods with fixed $H = 2$ nm and $R = 5$ nm.

in the HOMO energy, one can adjust the height to improve the overlap with H_2O redox potentials in a situation where the conduction band edge does not overlap with the $\text{H}_2/\text{H}_2\text{O}$ potential but the valence band edge does with the $\text{O}_2/\text{H}_2\text{O}$ potential.

B. Core-Shell InP-ZnTe Nanorods. Figure 9 delineates conduction and valence band edges along the radial direction in the plane of $z = 0$ for an InP-ZnTe nanorod with dimensions of $R = 5$ nm, $H = 10$ nm, and $R_1 = 2$ nm. The band alignment of this InP-ZnTe nanorod is type I, with similar valence band edges in the core and shell. Although the type-I band alignment does not favor a spatial separation between electrons and holes, the small offset in the valence band edges can be overcome by adjusting the dimensions to realize the desired electron-hole separation for hydrogen production.

Figures 10 and 11 describe P_{core} and the energies E_H , E_L , and E_g as a function of the core radius (R_1) in InP-ZnTe nanorods with a fixed height of $H = 2$ nm and an overall radius of $R = 5$ nm. We see from Figure 10 a similar phase transition as in the InP-CdS nanorods (Figure 3). For small core radii, strong quantum confinement squeezes the HOMO out of the core. Consequently, the HOMO and the LUMO are spatially separated with the LUMO in the core and the HOMO in the shell. For large core radii, however, the HOMO has a lower energy in the core and both the LUMO and the HOMO stay in the core. In the InP-ZnTe nanorods, charge distributions of both the HOMO and the LUMO strongly depend on R_1 , which is in contrast with the situation in the InP-CdS nanorods

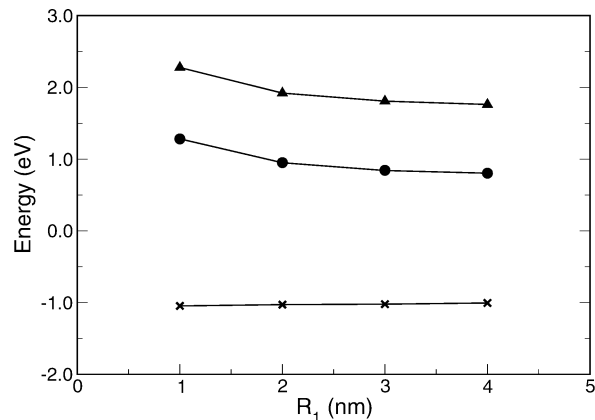


Figure 11. Energies of the HOMO (crosses) and the LUMO (circles) as well as the energy gap (E_g) (triangles) as a function of R_1 in the same structure as that in Figure 10.

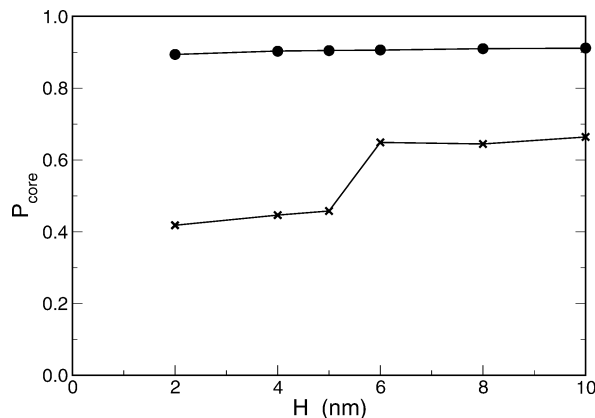


Figure 12. Integrated charge distribution in the core (P_{core}) for the HOMO (crosses) and the LUMO (circles) as a function of the height of core-shell InP-ZnTe nanorods with fixed $R_1 = 2$ nm and $R = 5$ nm.

described in Figure 5, where the charge distribution of the HOMO depends weakly on R_1 . This difference originates from the different band alignments illustrated in Figures 3 and 9. Because of the spatial separation of the LUMO and HOMO at small radii, Φ^2 , the square of the wave function overlap between the HOMO and the LUMO, decreases from 0.91 at $R_1 = 4$ nm to 0.44 at $R_1 = 1$, suggesting the recombination lifetime becomes twice longer. According to Figure 11, as the core radius decreases from $R_1 = 4$ nm to $R_1 = 1$ nm, the HOMO energy changes from -1.01 to -1.05 eV, while the LUMO energy changes from 0.80 to 1.28 eV. Thus, in the InP-ZnTe nanorods, the LUMO energy can be shifted notably, while the HOMO remains almost unchanged by adjusting the radial dimensions of the structures.

Interestingly, the phase transition of charge distribution also occurs as the height of the InP-ZnTe nanorods varies. Figure 12 shows how P_{core} depends on H of InP-ZnTe nanorods with fixed $R_1 = 2$ nm and $R = 5$ nm. According to Figure 12, for a structure with a height below 6 nm, the HOMO is mainly located in the shell and the HOMO and LUMO are spatially separated, while, for a structure with a height above 6 nm, the HOMO becomes localized in the core and therefore the HOMO and LUMO stay in the same region. The dependence of the energies E_H , E_L , and E_g on H in the same structures is illustrated in Figure 13. Again, as the height decreases from 10 to 2 nm, the LUMO energy change, from 0.69 to 0.95 eV, is much more pronounced than the HOMO energy change, from -0.97 to -1.03 eV.

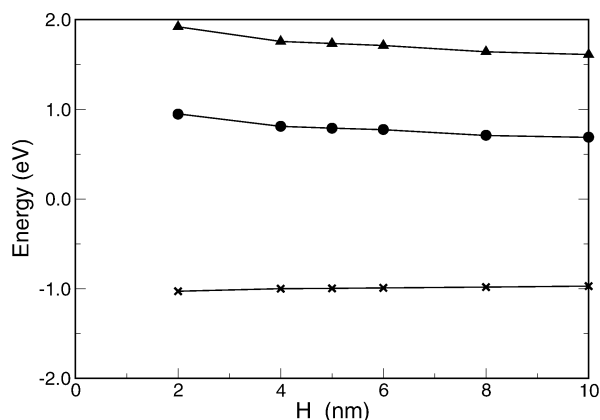


Figure 13. Energies of the HOMO (crosses) and LUMO (circles) as well as the energy gap (E_g) (triangles) as a function of H in the same structures as those in Figure 12.

V. Conclusions

We have systematically studied electronic structures and wave functions of core–shell nanorods using a strain-dependent k,p method. This study is aimed at identifying suitable semiconductor nanostructures as promising photoelectrodes for efficient PEC hydrogen production. We have shown that these core–shell nanorods exhibit a great tunability in terms of energies and wave function distributions by varying the dimensions of the structures. This tunability enables us to design nanostructures with proper materials and dimensions to meet the criteria for an efficient photoelectrode.

We have examined these nano-heterostructures against all of the criteria and found that core–shell InP–CdS and InP–ZnTe nanorods are especially promising photoelectrodes for efficient PEC hydrogen production. In these nanorods, photoexcitation happens in the core whose band gap matches the solar spectrum to maximize the solar-to-hydrogen efficiency. These nanorods are stable in the aqueous environment because the smaller band gap core is protected by the larger band gap shell from corrosion in water. The HOMO and LUMO in these structures can be localized in different regions, diminishing the probability of electron–hole recombination. This separation also accelerates the charge transfer from the photoelectrode into water and allows one to shift the HOMO and LUMO energies independently for achieving a desired overlap with the redox potentials in water.

InP–CdS and InP–ZnTe are especially good candidates for photoelectrodes because they have small discontinuities in the conduction and valence band edges, respectively. This allows one to effectively use quantum confinement and strain to achieve

electron–hole separation and energy modification of the HOMO and LUMO. In the InP–CdS nanorods, electrons are localized in the shell and holes in the core, whereas, in the InP–ZnTe structures, holes are localized in the shell and electrons in the core. Different electron–hole separation arrangements can be used under different aqueous conditions (e.g., different pH values) to achieve balanced electron and hole transfer rates, which is crucial for sustained hydrogen production.

Acknowledgment. We are grateful to S. Krishnamurthy for helpful discussions. This work was supported by the Department of Energy under contract DE-FC36-01GO11093.

References and Notes

- (1) Bard, A. J.; Fox, M. A. *Acc. Chem. Res.* **1995**, *28*, 141.
- (2) See, for example: Hagfeldt, A.; Grätzel, M. *Chem. Rev.* **1995**, *95*, 49.
- (3) Bansal, A.; Khaselev, O.; Turner, J. A. Photoelectrochemical system studies. In *Proceedings of the 2000 U.S. DOE hydrogen program review, NREL/CP-570-28890*, Golden, CO, May 8–10, 2000.
- (4) Varner, K.; Warren, S.; Turner, J. A. Photoelectrochemical systems for hydrogen production. In *Proceedings of the 2002 U.S. DOE hydrogen program review, NREL/CP-610-32405*, Golden, CO, May 6–10, 2002.
- (5) Finklea, H. A. *Semiconductor Electrodes*; Elsevier: Amsterdam, The Netherlands, 1998.
- (6) Khaselev, O.; Turner, J. A. *J. Electrochem. Soc.* **1991**, *316*, 57.
- (7) Kocha, S. S.; Turner, J. A. Nozik, A. J. *J. Electroanal. Chem.* **1994**, *27*, 367.
- (8) Kocha, S. S.; Turner, J. A. *J. Electrochem. Soc.* **1995**, *142*, 2625.
- (9) Chandrasekharan, N.; Kamat, P. V. *J. Phys. Chem. B* **2000**, *104*, 10851.
- (10) Kato, H.; Asakura, K.; Kudo, A. *J. Am. Chem. Soc.* **2003**, *125*, 3082.
- (11) Balet, L. P.; Ivanov, S. A.; Piryatinski, A.; Achermann, M.; Klimov, V. I. *Nano Lett.* **2004**, *4*, 1485.
- (12) Pokatilov, E. P.; Fonoberov, V. A.; Fomin, V. M.; Devreese, J. T. *Phys. Rev. B* **2001**, *64*, 245329.
- (13) Li, J.; Wang, L. W. *Appl. Phys. Lett.* **2004**, *84*, 3648.
- (14) Pryor, C.; *Phys. Rev. B* **1998**, *57*, 7190.
- (15) Landau, L. D.; Lifshitz, E. M. *Theory of Elasticity*; Pergamon: London, 1959.
- (16) Bahder, T. B. *Phys. Rev. B* **1990**, *41*, 11992.
- (17) Vurgaftman, I.; Meyer, J. R.; Ram-Mohan, L. R. *J. Appl. Phys.* **2001**, *89*, 5815.
- (18) Chen, A. B.; Sher, A. *Semiconductor Alloys*; Plenum: New York, 1995.
- (19) Lawaeta, P. *Phys. Rev. B* **1971**, *4*, 3460.
- (20) Hermann, C.; Weisbuch, C. *Phys. Rev. B* **1977**, *15*, 823.
- (21) Berlincourt, D.; Jaffe, H.; Shiozawa, L. R. *Phys. Rev.* **1963**, *129*, 1009.
- (22) Gavin, A.; Cardona, M. *Phys. Rev. B* **1970**, *1*, 672.
- (23) Martin, R. M. *Phys. Rev. B* **1972**, *6*, 4546.
- (24) Lucey, D. W.; MacRae, D. J.; Furis, M.; Sahoo, Y.; Cartwright, A. N.; Prasad, P. N. *Chem. Mater.* **2005**, *17*, 3754 and references therein.
- (25) Manciu, F. S.; Tallman, R. E.; McCombe, B. D.; Weinstein, B. A.; Lucey, D. W.; Sahoo, Y.; Prasad, P. N. *Physica E* **2004**, *26*, 14.